
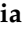


Article

# A Steady-State-Preserving Numerical Scheme for One-Dimensional Blood Flow Model

Carlos A. Vega <sup>1,\*</sup> , Sonia Valbuena <sup>2</sup>  and Jesús Blanco Bojato <sup>1</sup>

<sup>1</sup> Departamento de Matemáticas y Estadística, Universidad del Norte, Barranquilla 080001, Colombia; bojatoj@uninorte.edu.co

<sup>2</sup> Grupo de Investigación GIMED, Universidad del Atlántico, Barranquilla 080001, Colombia; soniabalbuena@mail.uniatlantico.edu.co

\* Correspondence: cvega@uninorte.edu.co

**Abstract:** In this work, an entropy-stable and well-balanced numerical scheme for a one-dimensional blood flow model is presented. Such a scheme was obtained from an explicit entropy-conservative flux along with a second-order discretisation of the source term by using centred finite differences. We prove that the scheme is entropy-stable and preserves steady-state solutions. In addition, some numerical examples are included to test the performance of the proposed scheme.

**Keywords:** one-dimensional blood flow model; balanced laws; entropy-stable scheme; steady-states

**MSC:** 65M06; 65M12; 65L04; 65Z05



**Citation:** Vega, C.A.; Valbuena, S.; Bojato, J.B. A Steady-State-Preserving Numerical Scheme for One-Dimensional Blood Flow Model. *Mathematics* **2024**, *12*, 407. <https://doi.org/10.3390/math12030407>

Academic Editors: Pengzhan Huang and Yinnian He

Received: 19 October 2023

Revised: 11 November 2023

Accepted: 16 November 2023

Published: 26 January 2024



**Copyright:** © 2024 by the authors. Licensee MDPI, Basel, Switzerland. This article is an open access article distributed under the terms and conditions of the Creative Commons Attribution (CC BY) license (<https://creativecommons.org/licenses/by/4.0/>).

## 1. Introduction

The mathematical modelling of blood flow in arteries has a long history, which can be traced back to the pioneering work of Euler [1]. Numerical simulations of blood flow have gained considerable importance in recent years because they provide non-invasive options to study and design effective medical procedures for treating some diseases. Although three-dimensional models are more complete in describing hemodynamic properties in greater detail, they are computationally expensive and depend on the accurate description of the boundary conditions. In this work, one-dimensional (1D) models were considered, which provide a realistic description of certain parts of the cardiovascular system and also provide boundary conditions for the more-complex three-dimensional models. Moreover, the predictive capabilities of (1D) blood flow models can be competitive with full (3D) models in the context of some specific hemodynamics conditions [2]. On the other hand, higher- and lower-dimensional models can be coupled in order to obtain a considerable reduction of the computational complexity [3].

There is a considerable amount of literature dealing with numerical solutions of one-dimensional blood flow models by using discontinuous Galerkin methods [4–8], finite-difference-weighted essentially non-oscillatory (WENO) schemes [9], Godunov-type schemes [10], and the arbitrary high-order derivatives (ADER) finite-volume framework [11]. Most of these references address the study of the well-balanced property using the hydrostatic reconstruction technique. More recently, a new and robust second-order well-balanced central-upwind scheme for (1D) blood flow models was developed in [12]. In this work, not only the well-balanced property was addressed, but also it was rigorously shown that the proposed scheme was entropy-stable.

The remainder of this paper is organised as follows. In Section 2, we recall the hyperbolic system of balance laws that describe the flow of blood and its properties. In Section 3, we describe the numerical methods to discretise the spatial derivative and the source term. Section 4 will be devoted to proving that the proposed scheme is entropy-stable and well-balanced. This section also includes numerical experiments demonstrating the performance of the scheme. Finally, some conclusions are drawn in Section 5.

## 2. Mathematical Model

The flow of blood in axisymmetric vessels with compliant walls and a flat velocity profile can be described by the following one-dimensional (1D) reduced model (see [4]):

$$\begin{cases} \frac{\partial A}{\partial t} + \frac{\partial(AU)}{\partial x} = 0 \\ \frac{\partial U}{\partial t} + U \frac{\partial U}{\partial x} + \frac{1}{\rho} \frac{\partial P}{\partial x} = \frac{\mathcal{F}}{\rho A}, \end{cases} \tag{1}$$

where  $A(x, t) = \pi R^2(x, t)$  is the cross-sectional area of the vessel at spatial position  $x$  and time  $t$  with  $R(x, t)$  being the radius,  $U(x, t)$  is the mean blood velocity in the axial direction,  $\rho$  is the blood density, assumed to be constant and equal to  $1060 \text{ kg/m}^3$ ,  $P = P(A)$  is the internal pressure, and  $\mathcal{F}(x, t)$  is the friction force per unit length. The present work is restricted to the inviscid limit where  $\mathcal{F} = 0$ .

Several expressions can be found in the literature to describe the pressure. In the present work, we used the algebraic expression proposed in [13]:

$$P = P_{ext} + \beta(\sqrt{A} - \sqrt{A_0}), \tag{2}$$

where the external pressure  $P_{ext}$ , the coefficient  $\beta$  stands for the arterial stiffness and is supposedly constant, and  $A_0 = A_0(x)$  is the vessel cross-sectional area at rest, which may be variable in the case of some pathologies.

We refer to Equation (1) as the system  $(A, U)$ . Such equations are an example of a *system of balance laws*:

$$\frac{\partial \mathbf{w}}{\partial t} + \frac{\partial \mathbf{f}(\mathbf{w})}{\partial x} = \mathbf{S}(\mathbf{w}) \tag{3}$$

where

$$\mathbf{w} = \begin{bmatrix} A \\ U \end{bmatrix}, \quad \mathbf{f}(\mathbf{w}) = \begin{bmatrix} AU \\ \frac{U^2}{2} + \frac{\beta\sqrt{A}}{\rho} \end{bmatrix}, \quad \mathbf{S}(\mathbf{w}) = \begin{bmatrix} 0 \\ \beta \frac{\partial \sqrt{A_0}}{\partial x} \end{bmatrix}$$

correspond to the vector of unknowns, flux function, and source term, respectively. In order to analyse the characteristic information, it is convenient to write the system in the non-conservative form:

$$\frac{\partial \mathbf{w}}{\partial t} + \mathbf{J}(\mathbf{w}) \frac{\partial \mathbf{w}}{\partial x} = \mathbf{S}(x, \mathbf{w}),$$

where

$$\mathbf{J}(\mathbf{w}) = \begin{bmatrix} U & A \\ c^2/A & U \end{bmatrix}$$

is the Jacobian matrix of the flux function with eigenvalues

$$\lambda_1 = U - c \quad \text{y} \quad \lambda_2 = U + c$$

and the corresponding right eigenvectors are given by

$$\mathbf{r}_1 = [-1, c/A]^\top \quad \text{y} \quad \mathbf{r}_2 = [1, c/A]^\top. \tag{4}$$

Here,  $c = \sqrt{\frac{\beta\sqrt{A}}{2\rho}}$  is the Moens–Korteweg wave speed.

It is well known that the solutions of balance laws may contain discontinuities, even for smooth initial data. Consequently, the solutions of such systems must be considered in the weak sense. Moreover, the weak solutions may not be unique, then it is necessary to impose an additional admissibility criterion or entropy conditions to select among the

possible solutions the one that is physically relevant [14]. In particular, the system  $(A, U)$  admits the entropy inequality:

$$\frac{\partial \hat{\eta}(\mathbf{w})}{\partial t} + \frac{\partial \hat{G}(\mathbf{w})}{\partial x} \leq 0, \tag{5}$$

where  $(\hat{\eta}, \hat{G})$  is the extended entropy pair introduced in [15]:

$$\hat{\eta} = \eta - \frac{\beta\sqrt{A_0}}{\rho} A, \hat{G} = G - \frac{\beta\sqrt{A_0}}{\rho} AU, \tag{6}$$

and  $(\eta, G)$  is the entropy pair  $(\eta, G)$  given by

$$\eta = \frac{1}{2}AU^2 + \frac{2\beta A^{3/2}}{3\rho}, G = \frac{1}{2}AU^3 + \frac{\beta UA^{3/2}}{\rho} \tag{7}$$

Using the entropy pair, we may obtain the entropy variables:

$$\mathbf{v}(\mathbf{w}) = \nabla \eta = \left[ \frac{U^2}{2} + \frac{\beta\sqrt{A}}{\rho}, AU \right]^T \tag{8}$$

with the corresponding entropy potential:

$$\psi(\mathbf{v}) := \mathbf{v}^T \mathbf{f}(\mathbf{w}(\mathbf{v})) - G(\mathbf{w}(\mathbf{v})) = \frac{AU^3}{2} + \frac{\beta UA^{3/2}}{\rho}. \tag{9}$$

In the extended case, we have

$$\hat{\mathbf{v}}(\mathbf{w}) = \nabla \hat{\eta} = \mathbf{v} - [\beta\sqrt{A_0}/\rho, 0]^T. \tag{10}$$

Systems such as (3) are of special interest because of the delicate balance that must exist between the convective term and the source term during the time evolution. Specifically, the steady-state solutions for the system (3) are the solutions  $\mathbf{w}(x)$ , which are time-independent. Thus, steady-state solutions satisfy the system:

$$\frac{\partial \mathbf{f}(\mathbf{w})}{\partial x} = \mathbf{S}(\mathbf{w}). \tag{11}$$

In particular, the system  $(A, U)$  admits the following steady-state solution, known as the *(non-zero-pressure) man-at-eternal-rest* steady-state or *dead-man equilibrium* [16]:

$$U = 0 \quad \text{y} \quad \sqrt{A} - \sqrt{A_0} = C = \text{constant}. \tag{12}$$

When  $C = 0$ , the *(zero-pressure) man-at-eternal-rest* steady-state is obtained, namely

$$U = 0 \quad \text{and} \quad A = A_0. \tag{13}$$

It is crucial that numerical methods to approximate steady-state solutions also satisfy a discrete version of (11). Such methods are termed *well-balanced schemes*.

### 3. Numerical Method

Since, in general, it is not possible to find an analytical solution of the system (3), it is imperative to approximate the solution numerically. To this end, we considered a semi-discrete finite-volume scheme for (3) on a uniform spatial mesh with nodes  $x_j = j\Delta x$ ,  $j \in \mathbb{Z}$ :

$$\frac{d\mathbf{w}_j(t)}{dt} = -\frac{1}{\Delta x} (\mathbf{F}_{j+1/2} - \mathbf{F}_{j-1/2}) + \mathbf{S}_j, \tag{14}$$

where  $w_j(t)$  is the cell average on  $I_j = [x_{j-1/2}, x_{j+1/2})$ ,  $F_{j+1/2}$  is the numerical flux associated with  $x_{j+1/2}$ , and  $S_j$  is a discretisation of the source term. It should be noted that the first term on the right-hand side corresponds to the discretisation of the spatial derivative  $-\mathbf{f}(\mathbf{w})_x$ . The discretisation of the time derivative will be discussed later.

The scheme (14) is *entropy-stable* with respect to the entropy pair  $(\hat{\eta}, \hat{G})$  if it satisfies a discrete version of the entropy inequality (5), that is

$$\frac{d}{dt} \hat{\eta}(\mathbf{w}_j(t)) + \frac{1}{\Delta x} (\hat{G}_{j+1/2} - \hat{G}_{j-1/2}) \leq 0 \tag{15}$$

for some *numerical entropy flux*  $\hat{G}_{j+1/2}$  consistent with the entropy flux  $\hat{G}$ . If the equality holds in (15), then the scheme (14) is called *entropy-conservative*.

From now on, we use

$$[[a]]_{j+1/2} := a_{j+1} - a_j, \quad \{\{a\}\}_{j+1/2} := \frac{1}{2}(a_{j+1} + a_j)$$

to denote, respectively, the jump of  $a$  across the interface  $x_{j+1/2}$  and the arithmetic mean of the  $a$  quantity.

In this work, we used a numerical flux of the form [17]:

$$\mathbf{F}_{j+1/2} = \tilde{\mathbf{F}}_{j+1/2} - \frac{1}{2} R_{j+1/2} \Lambda_{j+1/2} \langle\langle \mathbf{z} \rangle\rangle_{j+1/2}, \tag{16}$$

where:

- (i)  $\tilde{\mathbf{F}}_{j+1/2} = [\tilde{F}_{1,j+1/2}, \tilde{F}_{2,j+1/2}]^\top$  is the second-order and entropy-conservative flux for the homogeneous case of (3) given by

$$\tilde{F}_{1,j+1/2} = \{\{AU\}\}_{j+1/2}, \quad \tilde{F}_{2,j+1/2} = \frac{1}{2} \{\{U^2\}\}_{j+1/2} + \frac{\beta}{\rho} \{\{\sqrt{A}\}\}_{j+1/2}, \tag{17}$$

with the corresponding numerical entropy flux

$$\tilde{G}_{j+1/2} := \{\{\mathbf{v}^\top\}\}_{j+1/2} \tilde{\mathbf{F}}_{j+1/2} - \{\{\psi\}\}_{j+1/2}. \tag{18}$$

The numerical flux (17) was obtained in [18] from the condition (see [19]):

$$[[\mathbf{v}^\top]]_{j+1/2} \tilde{\mathbf{F}}_{j+1/2} = [[\psi]]_{j+1/2}. \tag{19}$$

- (ii)  $R_{j+1/2}$  is the matrix of right eigenvectors of the Jacobian matrix  $\mathbf{J}(\mathbf{w}_{j+1/2})$  being evaluated at the average state  $\mathbf{w}_{j+1/2} := (\mathbf{w}_j + \mathbf{w}_{j+1})/2$ ;  $\Lambda_{j+1/2} = \text{diag}(|\lambda_1|, |\lambda_2|)$  is a Roe-type matrix;  $\langle\langle \mathbf{z} \rangle\rangle_{j+1/2} = \mathbf{z}_{j+1/2}^+ - \mathbf{z}_{j+1/2}^-$ ,  $\mathbf{z}_{j+1/2}^-$  and  $\mathbf{z}_{j+1/2}^+$  denote, respectively, the left and right limiting values of the *scaled entropy variables*  $\mathbf{z} := R_{j+1/2}^\top \hat{\mathbf{v}}$  at interface  $x_{j+1/2}$ , obtained by the ENO reconstruction. The choice of this ENO method was due to the fact that it satisfies the so-called *sign property* [20]:

$$\text{sign}(\langle\langle \mathbf{z} \rangle\rangle_{j+1/2}) = \text{sign}([[\mathbf{z}]]_{j+1/2}), \tag{20}$$

which will be useful in proving the entropy stability of the flux (16).

The discretisation of the second component of the source term  $B(x) := \partial_x \sqrt{A_0(x)}$  is performed using the simple and well-known second-order centred difference approximation:

$$B'(x) \approx \frac{B(x + \Delta x) - B(x - \Delta x)}{2\Delta x}.$$

Thus, the discretisation of the source term yields

$$S_j = \frac{\beta}{\rho} \begin{bmatrix} 0 \\ B_{j+1} - B_{j-1} \\ 2\Delta x \end{bmatrix} \tag{21}$$

where  $B_j$  denotes the discrete approximation of  $B(x_j) = \sqrt{A_0(x_j)}$ .

#### 4. Theoretical Results and Numerical Experiments

In this section, it is shown that the scheme (14) with the numerical flux (16) and the discretisation of the source term (21) is entropy-stable and well-balanced. The proof is similar to that developed for the Saint-Venant equations and the relativistic magnetohydrodynamics equations in [21,22], respectively. Then, some examples are included to check that the numerical scheme verifies these properties at the discrete level.

**Theorem 1.** *The numerical scheme (14) with the numerical flux (16) and the discretisation of the source term (21) satisfies the following properties:*

- (i) *It is entropy-stable, i.e., it satisfies the discrete entropy inequality (15), where  $\hat{\eta}$  is the entropy function given by (6), and the corresponding numerical entropy flux is*

$$\hat{G}_{j+1/2} = \tilde{G}_{j+1/2} - \tilde{D}_{j+1/2} \tag{22}$$

with

$$\tilde{G}_{j+1/2} = \tilde{G}_{j+1/2} - \frac{\beta(B_j A_{j+1} U_{j+1} + B_{j+1} A_j U_j)}{2\rho}, \tag{23}$$

$$\tilde{D}_{j+1/2} = \frac{1}{2} \{ \{ \hat{\mathbf{v}}^T \} \}_{j+1/2} R_{j+1/2} \Lambda_{j+1/2} \langle \langle \mathbf{z} \rangle \rangle_{j+1/2}. \tag{24}$$

- (ii) *It preserves the discrete version of the man-at-eternal-rest (12); this means that, given the initial data:*

$$U_j = 0, \quad \sqrt{A_j} - B_j \equiv C \quad \forall j, \tag{25}$$

with  $C$  a constant, then the solution obtained with the scheme (14) satisfies

$$\frac{dw_j}{dt} = 0 \quad \forall j.$$

**Proof.** Let us first prove the entropy stability. Multiplying (14) by  $\hat{\mathbf{v}}_j^T$  yields

$$\hat{\mathbf{v}}_j^T \frac{d\mathbf{w}_j(t)}{dt} = -\frac{1}{\Delta x} \hat{\mathbf{v}}_j^T (\mathbf{F}_{j+1/2} - \mathbf{F}_{j-1/2}) + \hat{\mathbf{v}}_j^T \mathbf{S}_j \tag{26}$$

$$= -\frac{1}{\Delta x} \hat{\mathbf{v}}_j^T (\tilde{\mathbf{F}}_{j+1/2} - \tilde{\mathbf{F}}_{j-1/2}) \tag{27}$$

$$- \frac{1}{\Delta x} \hat{\mathbf{v}}_j^T \left( -\frac{1}{2} R_{j+1/2} \Lambda_{j+1/2} \langle \langle \mathbf{z} \rangle \rangle_{j+1/2} + \frac{1}{2} R_{j-1/2} \Lambda_{j-1/2} \langle \langle \mathbf{z} \rangle \rangle_{j-1/2} \right) \tag{28}$$

$$+ \hat{\mathbf{v}}_j^T \mathbf{S}_j \tag{29}$$

The left-hand side of (26) gives

$$\hat{\mathbf{v}}_j^T \frac{d\mathbf{w}_j}{dt} = \nabla \hat{\eta} \frac{d\mathbf{w}_j}{dt} = \frac{d\hat{\eta}(\mathbf{w}_j)}{dt}. \tag{30}$$

We now turn to the right-hand side. Using (10), the numerical flux  $\tilde{\mathbf{F}}_{j+1/2}$  explicitly given by (17), Equation (18), and the definition of  $\tilde{G}_{j+1/2}$  (18), we obtain

$$\begin{aligned}
 \widehat{\mathbf{v}}_j^\top (\widetilde{\mathbf{F}}_{j+1/2} - \widetilde{\mathbf{F}}_{j-1/2}) &= \mathbf{v}_j^\top (\widetilde{\mathbf{F}}_{j+1/2} - \widetilde{\mathbf{F}}_{j-1/2}) - [\beta B_j / \rho, 0] (\widetilde{\mathbf{F}}_{j+1/2} - \widetilde{\mathbf{F}}_{j-1/2}) \\
 &= \{\{\mathbf{v}^\top\}\}_{j+1/2} \widetilde{\mathbf{F}}_{j+1/2} - \frac{1}{2} \llbracket \mathbf{v}^\top \rrbracket_{j+1/2} \widetilde{\mathbf{F}}_{j+1/2} \\
 &\quad - \{\{\mathbf{v}^\top\}\}_{j-1/2} \widetilde{\mathbf{F}}_{j-1/2} - \frac{1}{2} \llbracket \mathbf{v}^\top \rrbracket_{j-1/2} \widetilde{\mathbf{F}}_{j-1/2} \\
 &\quad - \frac{\beta B_j}{\rho} (\{\{AU\}\}_{j+1/2} - \{\{AU\}\}_{j-1/2}) \\
 &= \{\{\mathbf{v}^\top\}\}_{j+1/2} \widetilde{\mathbf{F}}_{j+1/2} - \frac{1}{2} \llbracket \psi \rrbracket_{j+1/2} - \{\{\mathbf{v}^\top\}\}_{j-1/2} \widetilde{\mathbf{F}}_{j-1/2} - \frac{1}{2} \llbracket \psi \rrbracket_{j-1/2} \\
 &\quad - \frac{\beta}{2\rho} (B_j A_{j+1} U_{j+1} - B_j A_{j-1} U_{j-1}) \\
 &= \{\{\mathbf{v}^\top\}\}_{j+1/2} \widetilde{\mathbf{F}}_{j+1/2} - \{\{\psi\}\}_{j+1/2} - \{\{\mathbf{v}^\top\}\}_{j-1/2} \widetilde{\mathbf{F}}_{j-1/2} + \{\{\psi\}\}_{j-1/2} \\
 &\quad - \frac{\beta}{2\rho} (B_j A_{j+1} U_{j+1} - B_j A_{j-1} U_{j-1}) \\
 &= (\widetilde{\mathbf{G}}_{j+1/2} - \widetilde{\mathbf{G}}_{j-1/2}) - \frac{\beta}{2\rho} (B_j A_{j+1} U_{j+1} - B_j A_{j-1} U_{j-1}).
 \end{aligned} \tag{31}$$

To deal with the factor (28) in parenthesis, we took into account the definition of the scaled entropy variables and (24) to obtain

$$\begin{aligned}
 &-\frac{1}{2} \widehat{\mathbf{v}}_j^\top (R_{j+1/2} \Lambda_{j+1/2} \langle\langle \mathbf{z} \rangle\rangle_{j+1/2} - R_{j-1/2} \Lambda_{j-1/2} \langle\langle \mathbf{z} \rangle\rangle_{j-1/2}) \\
 &= -\frac{1}{2} \{\{\widehat{\mathbf{v}}^\top\}\}_{j+1/2} R_{j+1/2} \Lambda_{j+1/2} \langle\langle \mathbf{z} \rangle\rangle_{j+1/2} + \frac{1}{2} \{\{\widehat{\mathbf{v}}^\top\}\}_{j-1/2} R_{j-1/2} \Lambda_{j-1/2} \langle\langle \mathbf{z} \rangle\rangle_{j-1/2} \\
 &\quad + \frac{1}{4} \llbracket \widehat{\mathbf{v}}^\top \rrbracket_{j+1/2} R_{j+1/2} \Lambda_{j+1/2} \langle\langle \mathbf{z} \rangle\rangle_{j+1/2} + \frac{1}{4} \llbracket \widehat{\mathbf{v}}^\top \rrbracket_{j-1/2} R_{j-1/2} \Lambda_{j-1/2} \langle\langle \mathbf{z} \rangle\rangle_{j-1/2} \\
 &= -(\widetilde{\mathcal{D}}_{j+1/2} - \widetilde{\mathcal{D}}_{j-1/2}) + \frac{1}{4} \llbracket \mathbf{z}^\top \rrbracket_{j+1/2} \Lambda_{j+1/2} \langle\langle \mathbf{z} \rangle\rangle_{j+1/2} + \frac{1}{4} \llbracket \mathbf{z}^\top \rrbracket_{j-1/2} \Lambda_{j-1/2} \langle\langle \mathbf{z} \rangle\rangle_{j-1/2}
 \end{aligned} \tag{32}$$

Using the discretisation of the source term given by (21), we can rewrite (29) as

$$\begin{aligned}
 \widehat{\mathbf{v}}_j^\top \mathbf{S}_j &= (\mathbf{v}^\top - [\beta \sqrt{A_0} / \rho, 0]) \begin{bmatrix} 0 \\ \frac{\beta(B_{j+1} - B_{j-1})}{2\rho \Delta x} \end{bmatrix} \\
 &= \begin{bmatrix} \frac{U_j^2}{2} + \frac{\beta \sqrt{A_j}}{\rho}, A_j U_j \end{bmatrix} \begin{bmatrix} 0 \\ \frac{\beta(B_{j+1} - B_{j-1})}{2\rho \Delta x} \end{bmatrix} \\
 &= \frac{\beta}{2\rho \Delta x} (B_{j+1} A_j U_j - B_{j-1} A_j U_j).
 \end{aligned} \tag{33}$$

Inserting (30)–(33) into (26) and using the definition of  $\widetilde{\mathcal{G}}_{j+1/2}$  given by (22), we obtain

$$\begin{aligned} \frac{d\hat{\eta}(\mathbf{w}_j)}{dt} &= \\ &- \frac{1}{\Delta x} \left[ \left( \tilde{\mathcal{G}}_{j+1/2} - \frac{\beta(B_j A_{j+1} U_{j+1} + B_{j+1} A_j U_j)}{2\rho} \right) - \left( \tilde{\mathcal{G}}_{j-1/2} - \frac{\beta(B_{j-1} A_j U_j + B_j A_{j-1} U_{j-1})}{2\rho} \right) \right] \\ &+ \frac{1}{\Delta x} (\tilde{\mathcal{D}}_{j+1/2} - \tilde{\mathcal{D}}_{j-1/2}) - \frac{1}{4\Delta x} \llbracket \mathbf{z}^\top \rrbracket_{j+1/2} \Lambda_{j+1/2} \langle\langle \mathbf{z} \rangle\rangle_{j+1/2} - \frac{1}{4\Delta x} \llbracket \mathbf{z}^\top \rrbracket_{j-1/2} \Lambda_{j-1/2} \langle\langle \mathbf{z} \rangle\rangle_{j-1/2} \\ &= -\frac{1}{\Delta x} \left( (\tilde{\mathcal{G}}_{j+1/2} - \tilde{\mathcal{D}}_{j+1/2}) - (\tilde{\mathcal{G}}_{j-1/2} - \tilde{\mathcal{D}}_{j-1/2}) \right) \\ &- \frac{1}{4\Delta x} \left( \llbracket \mathbf{z}^\top \rrbracket_{j+1/2} \Lambda_{j+1/2} \langle\langle \mathbf{z} \rangle\rangle_{j+1/2} + \llbracket \mathbf{z}^\top \rrbracket_{j-1/2} \Lambda_{j-1/2} \langle\langle \mathbf{z} \rangle\rangle_{j-1/2} \right) \\ &= -\frac{1}{\Delta x} (\hat{\mathcal{G}}_{j+1/2} - \hat{\mathcal{G}}_{j-1/2}) - \frac{1}{4\Delta x} \left( \llbracket \mathbf{z}^\top \rrbracket_{j+1/2} \Lambda_{j+1/2} \langle\langle \mathbf{z} \rangle\rangle_{j+1/2} + \llbracket \mathbf{z}^\top \rrbracket_{j-1/2} \Lambda_{j-1/2} \langle\langle \mathbf{z} \rangle\rangle_{j-1/2} \right) \end{aligned}$$

Therefore,

$$\begin{aligned} \frac{d\hat{\eta}(\mathbf{w}_j)}{dt} + \frac{1}{\Delta x} (\hat{\mathcal{G}}_{j+1/2} - \hat{\mathcal{G}}_{j-1/2}) &= \\ &= -\frac{1}{4\Delta x} \left( \llbracket \mathbf{z}^\top \rrbracket_{j+1/2} \Lambda_{j+1/2} \langle\langle \mathbf{z} \rangle\rangle_{j+1/2} + \llbracket \mathbf{z}^\top \rrbracket_{j-1/2} \Lambda_{j-1/2} \langle\langle \mathbf{z} \rangle\rangle_{j-1/2} \right) \\ &\leq 0, \end{aligned}$$

where the last inequality is obtained by using the sign property. Summing up,

$$\frac{d\hat{\eta}(\mathbf{w}_j)}{dt} + \frac{1}{\Delta x} (\hat{\mathcal{G}}_{j+1/2} - \hat{\mathcal{G}}_{j-1/2}) \leq 0,$$

which proves the entropy stability.

We next show the second part of the theorem. From (25) it follows easily that

$$\tilde{\mathbf{F}}_{j+1/2} = \left[ 0, \frac{\beta}{\rho} \{\{\sqrt{A}\}\}_{j+1/2} \right]^\top, \quad \hat{\mathbf{v}}_j = \left[ \frac{\beta C}{\rho}, 0 \right]^\top.$$

The second equality implies that  $\hat{\mathbf{v}}_j$  is constant; thus,  $\langle\langle \mathbf{z} \rangle\rangle_{j+1/2} = \mathbf{0}$ , and consequently, the diffusion term in (16) vanishes. On account of this remark, we have  $\mathbf{F}_{j+1/2} = \tilde{\mathbf{F}}_{j+1/2}$ . Hence,

$$\begin{aligned} \frac{d\mathbf{w}_j(t)}{dt} &= -\frac{\beta}{\rho\Delta x} (\tilde{\mathbf{F}}_{j+1/2} - \tilde{\mathbf{F}}_{j-1/2}) + \mathbf{S}_j \\ &= -\frac{\beta}{\rho\Delta x} \begin{bmatrix} 0 \\ \{\{\sqrt{A}\}\}_{j+1/2} - \{\{\sqrt{A}\}\}_{j-1/2} \end{bmatrix} + \frac{\beta}{2\rho\Delta x} \begin{bmatrix} 0 \\ B_{j+1} - B_{j-1} \end{bmatrix} \\ &= -\frac{\beta}{2\rho\Delta x} \begin{bmatrix} 0 \\ (\sqrt{A}_{j+1} - B_{j+1}) - (\sqrt{A}_{j-1} - B_{j-1}) \end{bmatrix} \\ &= \begin{bmatrix} 0 \\ 0 \end{bmatrix}, \end{aligned}$$

the last equality being a consequence of (25).  $\square$

### 4.1. Time Discretisation

To discretise the temporal derivative in (14), the explicit second-order strong stability-preserving Runge–Kutta method (SSPRK) (Heun’s method) was used. This method is described by the following steps:

$$\begin{aligned} \mathbf{w}^{(1)} &= \mathbf{w}^n + \Delta t \mathcal{L}(\mathbf{w}^n), \\ \mathbf{w}^{(2)} &= \mathbf{w}^{(1)} + \Delta t \mathcal{L}(\mathbf{w}^{(1)}), \\ \mathbf{w}^{n+1} &= \frac{1}{2}(\mathbf{w}^n + \mathbf{w}^{(2)}), \end{aligned}$$

where

$$[\mathcal{L}(\mathbf{w})]_j := -\frac{1}{\Delta x} (\mathbf{F}_{j+1/2} - \mathbf{F}_{j-1/2}) + \mathbf{S}_j,$$

with  $\mathbf{F}_{j+1/2}$  and  $\mathbf{S}_j$  given by (16) and (21), respectively. In order to guarantee that the explicit scheme obtained is stable, the time and space discretisation steps must obey the CFL condition. For this purpose, the value of  $\Delta t$  is computed adaptively for each step. More exactly, the solution  $\mathbf{w}^{n+1}$  at  $t_{n+1} = t_n + \Delta t$  is calculated from  $\mathbf{w}^n$  by using the time step  $\Delta t = CFL * \Delta x / \alpha_{\max}^n$ , where  $\alpha_{\max}$  is an estimate of the maximal characteristic velocity for  $\mathbf{w}$ . All numerical experiments were carried out with a CFL number of 0.5.

### 4.2. Numerical Tests

In this section, some examples are presented to validate that the scheme correctly captures the steady-state solutions of System (1) and to verify that it is entropy-stable at the discrete level. In all examples, transmissive boundary conditions were imposed.

#### 4.2.1. Example 1

In the first example taken from [10], we considered three different configurations for the Riemann problem with the initial data:

$$\mathbf{w}(x, 0) = \begin{cases} \mathbf{w}_l = [A_l, U_l]^\top & \text{if } x \leq x_d \\ \mathbf{w}_r = [A_r, U_r]^\top & \text{if } x > x_d, \end{cases}$$

with the spatial domain of length  $L = 0.2$  m and  $x_d = 0.1$  m the point where the discontinuity is located. The numerical solutions were computed on a mesh with  $M = 200$  uniform cells, and for comparison purposes, reference solutions were computed on a refined mesh with 3200 uniform cells. The other parameters were  $A_0 = 3.14 \times 10^{-4}$  m<sup>2</sup>,  $\beta = 3.31 \times 10^6$  Pa/m along with different configurations of the initial data to obtain different types of waves. One can observe in Figure 1 the two rarefactions obtained at the final time  $t = 0.009$  s for the initial data  $\mathbf{w}_l = [2A_0, -1]^\top$ ,  $\mathbf{w}_r = [2A_0, 1]^\top$ . In Figure 2, it is observed that the scheme can capture the two shock waves obtained at the time  $t = 0.012$  s for the initial data  $\mathbf{w}_l = [A_0, 1]^\top$ ,  $\mathbf{w}_r = [2A_0, -1]^\top$ . The third configuration is  $\mathbf{w}_l = [A_0, 0]^\top$ ,  $\mathbf{w}_r = [2A_0, 0]^\top$ , and the results at the time  $t = 0.012$  s are displayed in Figure 3. In this case, the solutions develop a left discontinuity, followed by a right rarefaction. Due to the presence of two types of waves, we also present in Figure 4 the total entropy:

$$\mathcal{E}(t_n) := \Delta x \sum_{j=1}^M \eta(w_j(t_n)). \tag{34}$$

As expected, this quantity decreases over time, that is the scheme is entropy-stable at the discrete level.



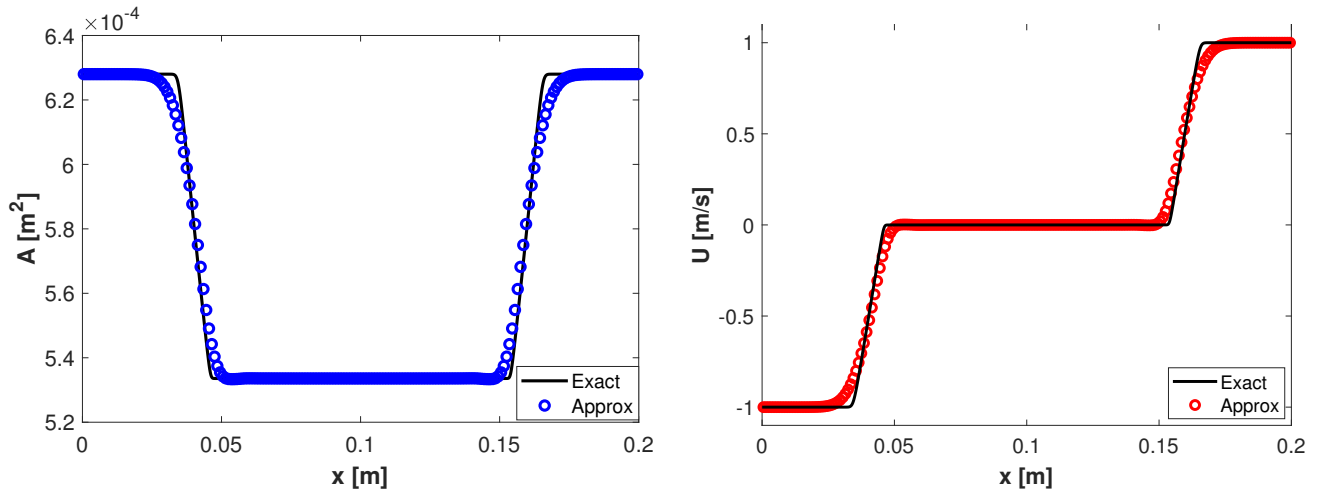


Figure 1. Rarefaction waves: area and velocity at  $t = 0.009$  s for the reference and approximate solutions.

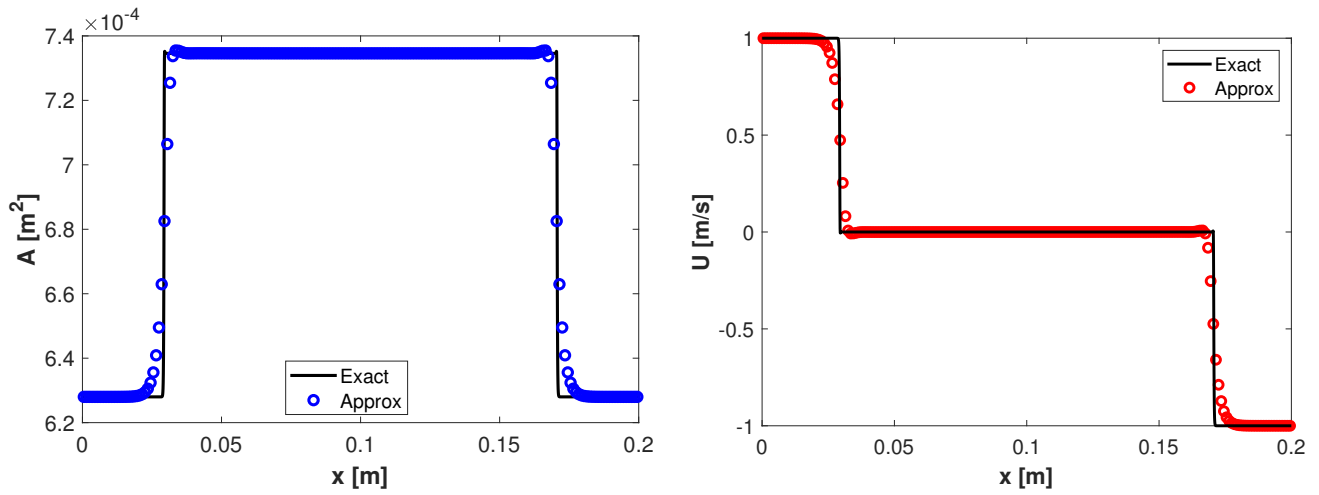


Figure 2. Shock waves: area and velocity at  $t = 0.012$  s for the references and approximate solutions.

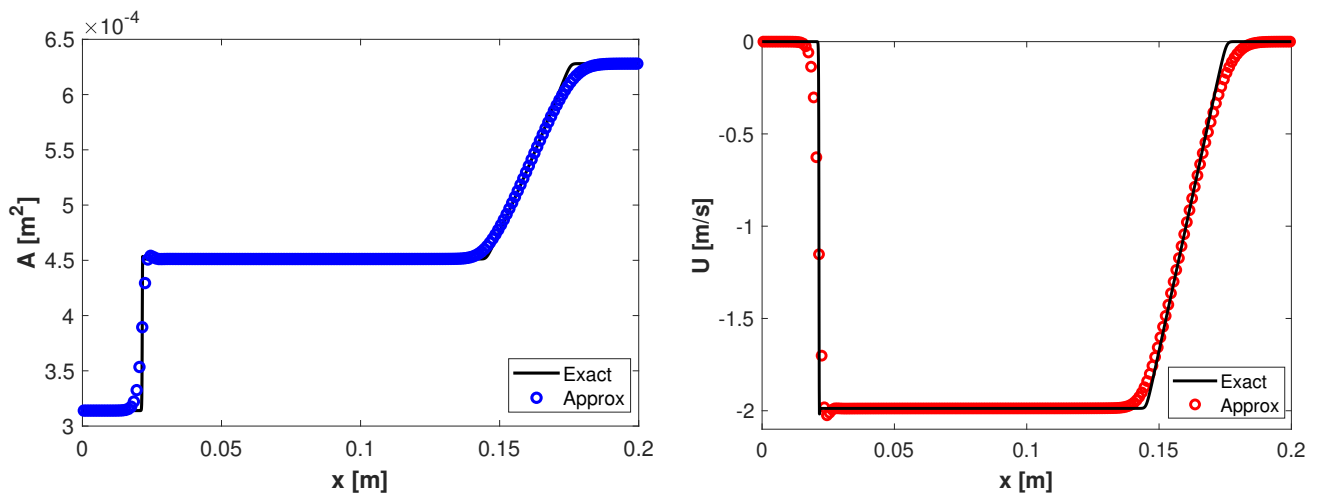


Figure 3. Shock and rarefaction waves: area and velocity at  $t = 0.012$  s for the references and approximate solutions.

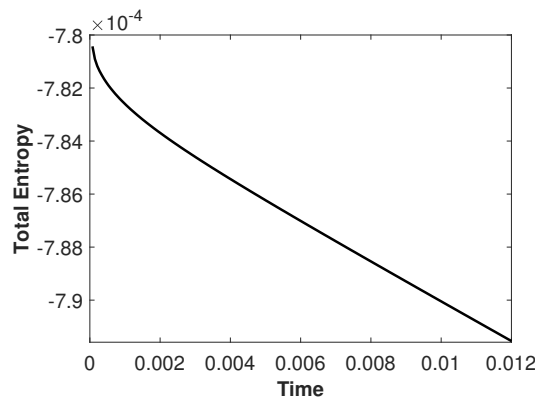


Figure 4. Entropy vs. time on a mesh with 200 uniform cells.

#### 4.2.2. Example 2

The purpose of this test problem taken from [5] was to check that the proposed scheme preserves the zero-pressure man-at-eternal-rest steady-state (13) at a discrete level. The configuration exhibited no flow and included a change in the section of the artery. This is the case for a dead man with an aneurysm. The initial conditions were  $U(x, 0) = 0$  and  $A(x, 0) = A_0(x) = \pi R_0^2(x)$ , where

$$R_0(x) = \begin{cases} \tilde{R} & \text{if } x \in [0, x_1] \cup [x_4, L], \\ \tilde{R} + \frac{\Delta R [\sin(\frac{x-x_1}{x_2-x_1} \pi - \frac{\pi}{2}) + 1]}{2} & \text{if } x \in ]x_1, x_2[, \\ \tilde{R} + \Delta R & \text{if } x \in [x_2, x_3], \\ \tilde{R} + \frac{\Delta R [\cos(\frac{x-x_3}{x_4-x_3} \pi) + 1]}{2} & \text{if } x \in ]x_3, x_4[, \end{cases}$$

with  $\tilde{R} = 4 \times 10^{-3}$  m,  $\Delta R = 1.0 \times 10^{-3}$  m,  $x_1 = 1.0 \times 10^{-2}$  m,  $x_2 = 3.05 \times 10^{-2}$  m,  $x_3 = 4.95 \times 10^{-2}$  m,  $x_4 = 7.0 \times 10^{-2}$  m, and  $L = 0.14$  m. The computational domain was  $[0, L]$  and  $\beta = \pi^{-1} \times 10^8$  Pa/m. The numerical results computed on a mesh with 200 cells at time  $t = 5$  s are plotted in Figure 5. In Figure 5 (left), it can be observed that the area remained the same as the area at rest, as expected. In Figure 5 (right), we compare the velocity obtained by using the well-balanced and entropy-stable (WB-ES) scheme proposed in this work and the velocity obtained by using the Lax–Friedrichs numerical flux combined with the discretisation of the source term given by (21). Notice that the WB-ES scheme preserved the steady-state exactly, while Lax–Friedrichs produced unacceptable spurious oscillations. These kind of anomalies were also reported before in [16].

#### 4.2.3. Example 3

This example (see [5]) corresponds to the case of a dead man with stenosis. Stenosis occurs when the artery narrows, and it leads to reduced blood flow from the heart to the rest of the body. The cross-sectional area at rest is  $A_0(x) = \pi R_0^2(x)$ , where

$$R_0(x) = \begin{cases} \tilde{R} + \Delta R & \text{for } x \in [0, x_1] \cup [x_4, L], \\ \tilde{R} - \frac{\Delta R}{2} \left( \sin\left(\frac{x-x_1}{x_2-x_1} \pi - \frac{\pi}{2}\right) - 1 \right) & \text{for } x \in (x_1, x_2), \\ \tilde{R} & \text{for } x \in [x_2, x_3], \\ \tilde{R} - \frac{\Delta R}{2} \left( \cos\left(\frac{x-x_3}{x_4-x_3} \pi\right) - 1 \right) & \text{for } x \in (x_3, x_4) \end{cases}$$

with  $\tilde{R} = 4 \times 10^{-3}$  m,  $\Delta R = 1.0 \times 10^{-3}$  m, an artery of length  $L = 0.14$  m,  $x_1 = 9L/40$ ,  $x_2 = L/4$ ,  $x_3 = 3L/40$ , and  $x_4 = 31L/40$ . The initial conditions are

$$A(x,0) = (C + \pi^{1/2}R_0(x))^2, \quad U(x,0) = 0,$$

where  $C = 10^{-3}$  m.

The numerical solutions were computed at  $t = 1$  s on three different meshes:  $M = 100$ ,  $M = 200$ , and  $M = 400$ . As observed in Figure 6, the proposed scheme preserved the steady-state (12) at the discrete level, i.e., the quantity  $\sqrt{A(x,t)} - \sqrt{A_0(x)}$  remained constant, and the velocity was null.

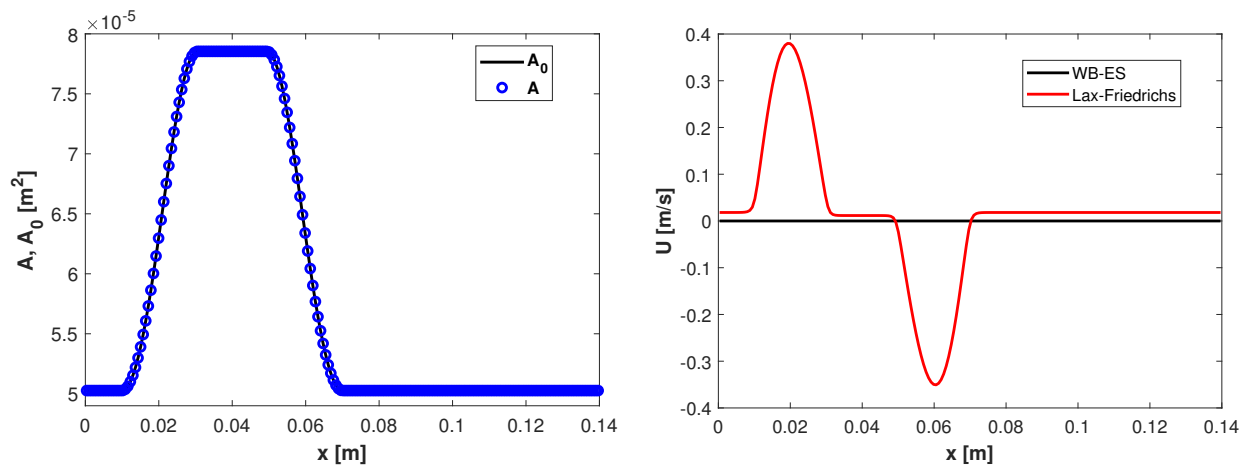


Figure 5. Numerical solutions of the zero-pressure man-at-eternal-rest problem on a mesh with 200 cells at time  $t = 5$  s. Area and area at rest (left) and comparison between solutions obtained with WB-ES and Lax-Friedrichs schemes (right).

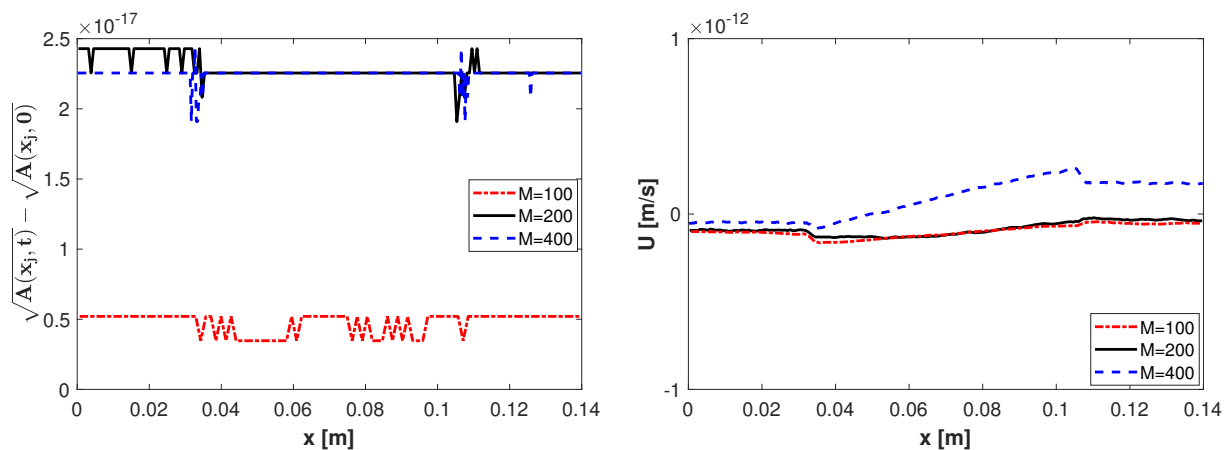


Figure 6. Area minus area at rest (left) and velocity (right) for the non-zero-pressure man-at-eternal-rest problem at  $t = 1$  s on three different meshes:  $M = 100$ ,  $M = 200$ , and  $M = 400$ .

### 5. Conclusions

We presented a numerical scheme to approximate the solutions of a blood flow model in arteries. It was shown analytically that the scheme is entropy-stable and preserves the steady-state solutions. These properties were also tested numerically with some standard examples. Although higher-order schemes can be found in the literature related to the numerical approximation of blood flows, the value of the second-order discretisation of the source term proposed in this work lies in the fact that, using linear combinations of them combined with high-order entropy-stable fluxes, it is possible to construct arbitrarily high-order entropy-stable schemes that preserve the steady-state solutions.

**Author Contributions:** Conceptualisation, S.V., C.A.V. and J.B.B.; formal analysis, C.A.V.; investigation, S.V. and C.A.V.; software, validation and supervision, C.A.V. and J.B.B.; writing—original draft, C.A.V.; writing—review and editing, S.V. and C.A.V. All authors have read and agreed to the published version of the manuscript.

**Funding:** This research received no external funding.

**Data Availability Statement:** Data are contained within the article.

**Acknowledgments:** The authors wish to express his thanks to the anonymous reviewers for their valuable comments and feedback.

**Conflicts of Interest:** The authors declare no conflict of interest.

## References

1. Euler L. Principia pro motu sanguinis per arterias determinando. *Opera Posthuma* **1862**, *2*, 814–823.
2. Blanco, P.J.; Bulant, C.A.; Müller, L.O.; Maso Talou G.D.; Guedes Bezerra C.; Lemoas, P.A.; Feijóo R.A. Comparison of 1D and 3D Models for the Estimation of Fractional Flow Reserve. *Sci. Rep.* **2018**, *8*, 17275. [[CrossRef](#)]
3. Formaggia L.; Gerbeau, J.F.; Nobile, F.; Quarteroni, A. On the coupling of 3D and 1D Navier-Stokes equations for flow problems in compliant vessels. *Comput. Methods Appl. Mech. Engrg.* **2001**, *191*, 561–582. [[CrossRef](#)]
4. Sherwin, S.J.; Franke, V.; Peiró, J.; Parker, K. One-dimensional modelling of a vascular network in space–time variables. *J. Eng. Math.* **2003**, *47*, 217–250. [[CrossRef](#)]
5. Britton J.; Xing, Y. Well-balanced discontinuous Galerkin methods for the one-dimensional blood flow through arteries model with man-at-eternal-rest and living-man equilibria. *Comput. Fluids* **2020**, *203*, 104493. [[CrossRef](#)]
6. Li, G.; Delestre, O.; Yuan Y. Well-balanced discontinuous Galerkin method and finite volume WENO scheme based on hydrostatic reconstruction for blood flow model in arteries. *Int. J. Numer. Methods Fluids* **2020**, *86*, 491–508. [[CrossRef](#)]
7. Puelz, C.; Canic S.; Rivière, B.; Rusin, C.G. Comparison of reduced models for blood flow using Runge-Kutta discontinuous Galerkin methods. *Appl. Numer. Math.* **2017**, *115*, 114–141. [[CrossRef](#)]
8. Valbuena, S.; Vega, C.A. Numerical approximation of living-man steady-state solutions for blood flow in arteries using a well-balanced discontinuous Galerkin scheme. *Results Appl. Math.* **2023**, *18*, 100375. [[CrossRef](#)]
9. Wang, Z.; Li, G.; Delestre O. Well-balanced finite difference weighted essentially non-oscillatory schemes for the blood flow model. *Int. J. Numer. Methods Fluids* **2016**, *82*, 607–622. [[CrossRef](#)]
10. Guitti, B.; Berton, C.; Hoang, M.; Toro, E. A fully well-balanced scheme for the 1D blood flow equations with friction source term. *J. Comput. Phys.* **2020**, *421*, 109750. [[CrossRef](#)]
11. Müller L.O.; Parés, C.; Toro, E. Well-balanced high-order numerical schemes for one-dimensional blood flow in vessels with varying mechanical properties. *J. Comput. Phys.* **2013**, *242*, 53–85. [[CrossRef](#)]
12. Chu, S.; Kurganov A. Flux globalization based well-balanced central-upwind scheme for one-dimensional blood flow models. *Calcolo*, **2023**, *60*, 2. [[CrossRef](#)]
13. Formaggia, L.; Nobile, F.; Quarteroni, A.; Veneziani, A. Multiscale modelling of the circulatory system: A preliminar analysis. *Comput. Vis. Sci.* **1999**, *2*, 75–83. [[CrossRef](#)]
14. Dafermos, C. *Hyperbolic Conservation Laws in Continuum Physics*; Springer: Berlin/Heidelberg, Germany, 2000.
15. Guigo, A.R.; Delestre, O.; Fullana, J.M.; Lagrée P.Y. Low-Shapiro hydrostatic reconstruction technique for blood flow simulation in large arteries with varying geometrical and mechanical properties. *J. Comput. Phys.* **2017**, *331*, 108–136. [[CrossRef](#)]
16. Delestre, O.; Lagrée, P.Y. A ‘well-balanced’ finite-volume scheme for blood flow simulation. *Int. J. Numer. Methods Fluids.* **2013**, *72*, 177–205. [[CrossRef](#)]
17. Fjordholm, U.S.; Mishra, S.; Tadmor, E. Arbitrary high-order essentially non-oscillatory entropy-stable schemes for systems of conservation laws. *SIAM J. Numer. Anal.* **2012**, *50*, 544–573. [[CrossRef](#)]
18. Bürger, R.; Valbuena, S.; Vega, C. A well-balanced and entropy-stable scheme for a reduced blood flow model. *Numer. Meth. Part Differ. Equ.* **2023**, *39*, 2491–2509. [[CrossRef](#)]
19. Tadmor, E. The numerical viscosity of entropy-stable schemes for systems of conservation laws, I. *Math. Comput.* **1987**, *49*, 91–103. [[CrossRef](#)]
20. Fjordholm, U.S.; Mishra, S.; Tadmor E. ENO reconstruction and ENO interpolation are stable. *Found. Comput. Math.* **2013**, *13*, 139–159. [[CrossRef](#)]
21. Fjordholm, U.S.; Mishra, S.; Tadmor E. Well-balanced and energy stable schemes for the shallow water equations with discontinuous topography. *J. Comput. Phys.* **2011**, *230*, 5587–5609. [[CrossRef](#)]
22. Wu K.; Shu, C.W. Entropy Symmetrization and High-Order Accurate Entropy Stable Numerical Schemes for Relativistic MHD Equations. *SIAM J. Sci. Comput.* **2020**, *42*, A2230–A2261. [[CrossRef](#)]

**Disclaimer/Publisher’s Note:** The statements, opinions and data contained in all publications are solely those of the individual author(s) and contributor(s) and not of MDPI and/or the editor(s). MDPI and/or the editor(s) disclaim responsibility for any injury to people or property resulting from any ideas, methods, instructions or products referred to in the content.